LANGMUIR

pubs.acs.org/Langmuir
Article

Formation and Characterization of Stable Antifouling Colloidal Particles via Surface-Initiated-Photoinduced Electron Transfer-Reversible Addition–Fragmentation Chain-Transfer Polymerization for Standardized Biophysical Measurements

Jelle B.J. van den Beukel,* Barend van Lagen, Han Zuilhof,* and Edwin van der Pol

Cite This: *Langmuir* 2025, 41, 33751–33760

ABSTRACT: Extracellular vesicles (EVs) are potential biomarkers for various diseases, but EV concentration measurements are difficult to achieve, which often leads to incomparable and irreproducible data. To solve this problem, colloidal particles of known concentration could assist in tracking the sample dilution and determining the volume of the sample in which EVs are counted during the analysis. However, colloidal particles in body fluids suffer from instability due to the nonspecific adsorption of proteins onto their surface. Our aim is to functionalize colloidal particles with antifouling polymer brushes to prevent nonspecific adsorption of proteins from body fluids. To functionalize polystyrene colloidal particles with a diameter of 220 nm, surface-initiated photoinduced electron transfer-reversible addition–fragmentation chain-transfer polymerization was used with three different monomers: nonzwitterionic *N*-(2-hydroxypropyl)-methacrylamide (HPMA), zwitterionic methacrylate phosphocholine, and carboxybetaine methacrylate. Polymer brush growth was confirmed with dynamic light scattering, X-ray photoelectron spectroscopy, and transmission electron microscopy. The functionalized colloidal particles were exposed to a single-protein solution and human blood plasma, wherein HPMA-functionalized colloidal particles demonstrated excellent antifouling. Moreover, HPMA-functionalized colloidal particles were added to pure plasma and remained stable for at least 5 h. The successful functionalization of colloidal particles with antifouling polymer brushes shows great potential for further research in both flow cytometry and biomedical applications, particularly in selective biomarker detection.

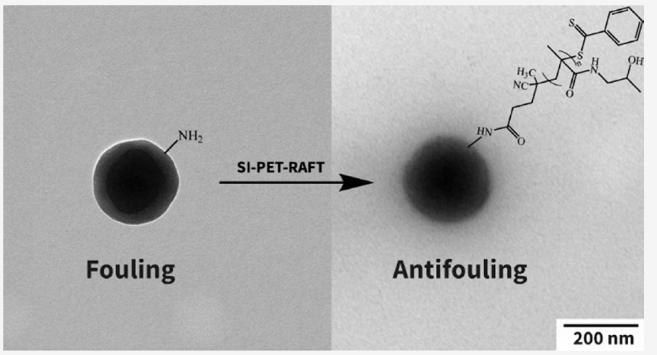

INTRODUCTION

Extracellular vesicles (EVs) are biological nanoparticles released by cells into body fluids, such as human blood plasma.[1−4] As the composition and concentration of EVs change during disease, EVs are potential biomarkers for various diseases.[1,2,4] However, due to the submicrometer dimensions[5] and complex environment of EVs,[6] as well as the preanalytical and analytical variables involved in EV measurements,[7,8] reliable EV concentration measurements are difficult to achieve. Consequently, published data on EV concentrations are typically incomparable and often also irreproducible.[5,9]

One potential solution to improve the reliability of EV concentration measurements is the use of inert colloidal particles with a known concentration, which can be spiked into samples before applying any preanalytical procedure. Such colloidal particles could assist in tracking the sample dilution and determining the volume of sample in which EVs are counted during the analysis. While colloidal particles of various concentrations, materials, and sizes are available, they all suffer from the same issue: instability. In complex body fluids like plasma, proteins will nonspecifically adsorb onto colloidal particles, leading to biofouling. Biofouling yields a protein corona around the colloidal particle.[10−14] The composition of this protein corona depends on the temperature, biological medium, material, morphology, and surface chemistry of the colloidal particles,[15−17] and overall significantly affects the morphology of the colloidal particle. Generally, fouling leads to particle aggregation and reduced stability in biological fluids.

Research has focused on preventing protein fouling by introducing antifouling coatings that inhibit protein attachment. These antifouling coatings, often composed of polymer brushes grafted onto or from a solid surface, can offer excellent antifouling capabilities.[18−23] Although these coatings are

Received: July 2, 2025
Revised: October 28, 2025
Accepted: October 28, 2025
Published: December 12, 2025

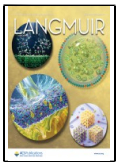

https://doi.org/10.1021/acs.langmuir.5c03234
Langmuir 2025, 41, 33751−33760

Scheme 1. Synthesis of Water-Soluble RAFT Agent and SI-PET-RAFT Functionalization of Colloidal Particles[a]

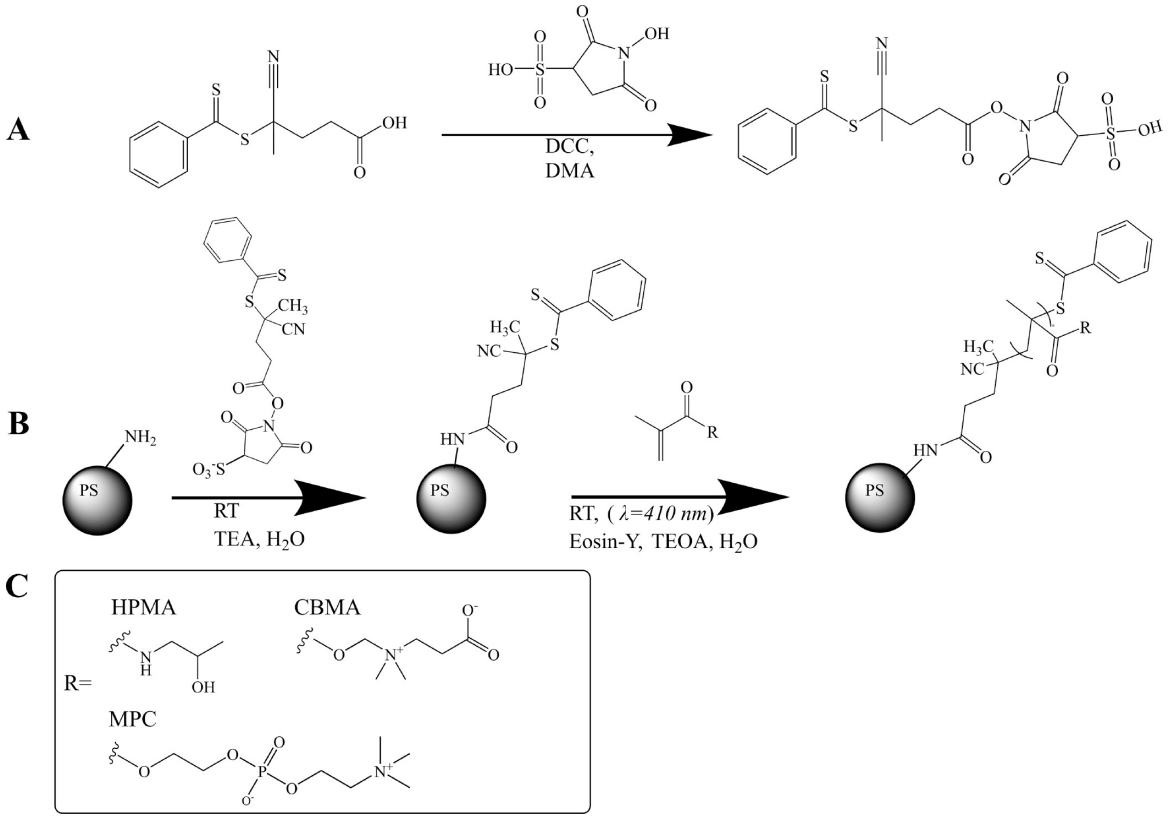

[a](A) Synthesis of sulfo-NHS CPP. (B) Functionalization of PS-NH_2 cores with polymer brushes. (C) Monomers used for the functionalization of the colloidal particles.

typically applied to flat surfaces, they have also been introduced onto colloidal particles.[24−26] The application of antifouling coatings onto colloidal particles has been successfully achieved using both reversible addition−fragmentation chain transfer (RAFT),[24] and atom transfer radical polymerization (ATRP).[25,26] However, conventional RAFT and ATRP require organic solvents and oxygen-free conditions, making the technique difficult to use by nonchemists and in mass production.

To address these limitations, Hawker and Fors proposed a photoinduced living polymerization,[27] for which eventually a reductive quenching cycle was developed using Eosin-Y with triethanolamine (TEOA) as a sacrificial electron donor to scavenge oxygen from the polymerization system. This method was further optimized by Kuzmyn et al., who introduced a method of growing polymer brushes from surfaces using surface-initiated photoinduced-electron-transfer reversible-addition−fragmentation-transfer (SI-PET-RAFT).[21] The thickness of such brushes can be controlled via the irradiation time[21,22] and in principle even increased to >250 nm under flow conditions.[28] SI-PET-RAFT enables polymer brush growth in aqueous environments under standard atmospheric conditions, making it an ideal technique for mass production.

In this study, three different monomers were selected based on their previously demonstrated antifouling properties: the nonzwitterionic monomer N-(2-hydroxypropyl)methacrylamide (HPMA), the zwitterionic monomers methacrylate phosphocholine (MPC), and carboxybetaine methacrylate (CBMA) (Scheme 1).[21,26] Zwitterionic monomers carry both cationic and anionic groups, which makes them very hydrophilic, increasing antifouling behavior when applied to a surface.[23] Also, HPMA has shown excellent antifouling properties, although the mode of action is not precisely known.[21,26,29] Van Andel et al. performed preliminary quantum chemical calculations to show that strong hydrogen bond bridges tightly bind water molecules to HPMA, suggesting antifouling behavior.[26] Polystyrene was chosen as the core material of the colloidal particle, as polystyrene particles (1) are widely available in size ranges comparable to EVs, (2) display neutral buoyancy within EV size ranges, and (3) have a high refractive index and thus light scattering efficiency compared to EVs. The efficient light scattering improves the differentiation between colloidal particles and EVs by optical detection methods.

In this paper, we describe the synthesis, characterization, and use of antifouling colloidal particles. First, we present the synthesis of a water-soluble RAFT agent (Scheme 1A). Next, polystyrene colloidal particles were functionalized with antifouling polymer brushes using this water-soluble RAFT agent (SI-PET-RAFT (Scheme 1B). The resulting functionalized colloidal particles were characterized in detail by dynamic light scattering, X-ray photoelectron spectroscopy, and transmission electron microscopy. Finally, we validated the antifouling properties and stability of the colloidal particles upon exposure to various complex biological fluids.

EXPERIMENTAL SECTION

Materials. All reagents were used without further purification unless otherwise specified. *N,N*-dimethylacetamide (DMA), diethyl ether, *N,N*-dicyclohexylcarbodiimide (DCC), triethylamine (TEA),

https://doi.org/10.1021/acs.langmuir.5c03234
Langmuir 2025, 41, 33751−33760

triethanolamine (TEOA), Pur-A-Lyzer Maxi Dialysis kit (capacity 0.1−3 mL, molecular weight cutoff 12−14 kDa), centrifugal filtration tubes (10 kDa, Millipore, Germany), and bovine albumin-fluorescein isothiocyanate conjugate (BSA-FITC) were purchased from Sigma-Aldrich (The Netherlands). 4-Cyano-4-(phenylcarbonothioylthio)-pentanoic acid (CPPA), *N*-hydroxysulfosuccinimide sodium salt (Sulfo-NHS), *N*-(2-hydroxypropyl)methacrylamide (HPMA), 2-(methacryloyloxy)ethyl 2-(trimethylammonio)ethyl phosphate (MPC), 3-[[2-(methacryloyloxy)ethyl]dimethylammonio] propionate (CBMA), and eosin-Y were purchased from TCI chemicals Europe (Belgium). DiagPoly Amine polystyrene particles (DNM-F001, 0.2 μm, 25% w/w, ∼4−5 E12 particles/mL) (PS-NH_2) were purchased from CD-Bioparticles, USA. AnaTag HiLyte Fluor 488 Protein labeling kit was purchased from AnaSpec, USA. Gold-coated silicon wafers (100 mm, 200 nm Au coating) were purchased from SSens, The Netherlands. Deionized water was obtained from a Milli-Q integral 3 system (Millipore, Molsheim, France; Milli-Q water). Dulbecco's phosphate-buffered saline (DPBS) was purchased from Corning Life Sciences.

Blood Collection and Plasma Preparation. Blood collection was performed according to the guidelines of the Amsterdam Medical Centre, University of Amsterdam, medical ethical committee (W22−243 #22.298). Blood was collected from 20 healthy volunteers (10 male and 10 female). One tube of EDTA blood (BD Vacutainer blood collection tubes, USA) was collected per volunteer. To prepare plasma, blood was centrifuged for 15 min at 2500 g at 20 °C. Plasma was collected in a new tube, leaving 1 cm of plasma above the buffy coat. The plasma was centrifuged again at 2500 g for 15 min at 20 °C, transferring the plasma into an EDTA collection tube, leaving 1 cm of plasma above the bottom of the tube. All EDTA plasma was pooled together and aliquoted into plasma portions of 100 μL before being flash-frozen in liquid nitrogen for 15 min. Plasma aliquots were stored at −80 °C before use. Plasma was thawed in a water bath at 37 °C before use.

Light Source. To polymerize samples by irradiation, light-emitting diodes (LEDs) with a maximum intensity at 410 nm (Intelligent LED solutions (United Kingdom) product number ILS-XN05-S400−0058-SC211-W2) were used. LED drivers (MEAN WELL (The Netherlands) product number: LCM-40DA) were used to apply a current of 700 mA through the LEDs, resulting in a radiometric output power of 2000 mW, according to manufacturer specifications.

Synthesis of Functionalized Colloidal Particles. Functionalized colloidal particles were synthesized according to Scheme 1.

Synthesis of Water-Soluble RAFT Agent. To improve the water solubility of the RAFT agent, a sulfo-NHS variant was synthesized (Scheme 1A). DMA was bubbled with argon gas and cooled in an ice bath for 30 min before use. DMA (20 mL), the RAFT agent, cyano-4-(phenylcarbonothioylthio)pentanoic acid (CPPA; 279 mg, 1 mmol, 1 equiv), and sulfo-NHS (434 mg, 2 mmol, 2 equiv) were added to a round-bottom flask. The flask was placed in an ice bath and capped with a septum and a balloon containing argon gas. The solution was stirred for 30 min to dissolve all of the reagents. Meanwhile, in a separate vial, DCC (619 mg, 3 mmol, 3 equiv) was dissolved in 5 mL of DMA. The DCC solution was added through the septum, and the solution was left to react for 24 h while slowly heating it up to room temperature. After 24 h, the stirring was stopped and the flask was placed in an ice bath. The urea byproduct was filtered off using a Buchner filter. The pink filtrate, which contains the sulfo-NHS-CPP product, was precipitated by using ice-cold diethyl ether and collected via centrifugation at 2500*g*. The precipitate was dissolved in DMA and precipitation was repeated thrice. Afterward, the pink precipitate was dissolved in Milli-Q water and lyophilized, resulting in crude sulfo-NHS-CPP (545 mg) as a dark pink powder. Sulfo-NHS-CPP was used for the RAFT-functionalization of colloidal particles without further purification. Remaining sulfo-NHS does not interfere with future functionalization of the PS particles.

RAFT Functionalization of Colloidal Particles. Sulfo-NHS-CPP was first used to functionalize the colloidal particles with the desired RAFT-agent (Scheme 1B). Sulfo-NHS-CPP (11 mg) was dissolved in Milli-Q water (900 μL) in an Eppendorf tube. Next, PS-NH_2 colloidal particles (100 μL of a 25% (w/w) solution, 220 nm in diameter) were added, and the contents were mixed before adding TEA (10 μL, 72 μmol). The tube was placed on an end-over-end shaker to ensure proper mixing at 20 rpm. After 90 min the contents were dialyzed (12−14 kDa membrane, 0.1−3 mL tube size) against Milli-Q water for 24 h, refreshing the Milli-Q water after 4 h, while the sample was covered with aluminum foil to protect the sample from light. After 24 h of dialysis, the resulting PS-CPP colloidal particles were immediately used for further polymerization.

SI-PET-RAFT Polymerization on Colloidal Particles. Polymerization on the PS-CPP colloidal particles was performed via SI-PET-RAFT following a procedure adapted from Kuzmyn et al.[21] (Scheme 1B). A stock solution of Eosin-Y photo catalyst was prepared, containing eosin-Y (25 mg, 39 μmol) and TEOA (160 mg, 1.6 mmol) dissolved in Milli-Q water (10 mL). To realize the three different colloidal particle coatings, monomer (HPMA, 180 mg, 1.3 mmol), MPC (89 mg, 0.3 mmol), or CBMA (138 mg, 0.6 mmol) was added together with functionalized PS-CPP (1 mL of a 2.5% w/w solution) and a magnetic stir bar to a borosilicate glass vial. Contents were mixed before the addition of eosin-Y stock solution (10 μL). The vial was constantly stirred while irradiated by the LED source from a 3 cm distance. After reaction times of 30 min for HPMA, 15 min for MPC, and 5 min for CBMA, polymerization was stopped by removing the vial from the light source. Reaction times were optimized to yield polymer brush lengths of 15−20 nm. The functionalized colloidal particles (1 mL total volume) were then washed via centrifugation at 18,000*g* for 10 min. 900 μL of supernatant was removed, and the pellet was dispersed in 900 μL of fresh Milli-Q water. Dispersion was assisted by sonication at 37 Hz for 1 min. Washing was repeated three times before the colloidal particles were stored at 4 °C.

Characterization. *X-ray Photoelectron Spectroscopy (XPS).* Functionalized colloidal particles (30 μL) were drop-cast on a plasma-cleaned piece of a 200 nm-thick gold-coated Si wafer and dried in a vacuum oven at 30 °C for 1 h. The drop-cast colloidal particles were then analyzed using a JPS-9200 photoelectron spectrometer (JEOL Ltd., Japan). Spectra were obtained using monochromatic Al Kα X-ray radiation at 12 kV and 20 mA with an analyzer energy pass of 10 eV for narrow scans. The obtained spectra were processed using the CASA XPS peak fit program (version 2.3.24 PR 1.0).[30] A peak fitting restraint of full-width-half-maximum (fwhm) was placed for A*1, resulting in all peaks being constant in their fwhm.

Dynamic Light Scattering (DLS). DLS was measured on a Zetasizer Nano-ZS (Malvern Panalytical, United Kingdom) equipped with a He−Ne laser operating at a wavelength of 633 nm. Functionalized colloidal particles were diluted 1000-fold in Milli-Q water before measuring. Measurements were performed at 21 °C using a 120 s equilibrium time with 5 runs of 15 scans. Measurements were acquired using Zetasizer Malvern (version 8.02) using a non-negatively constrained least-squares fitting algorithm for the analysis of the decorrelation curve.

Microfluidic Resistive Pulse Sensing (MRPS). The size distribution and concentration of functionalized colloidal particles were measured by MRPS (nCS1, v0, Spectradyne, USA). Samples were diluted 100 to 1000-fold before loading 6 μL sample to C900 cartridges, which have a detection range of 130−900 nm. The nCS1 viewer software (version 2.5.0.325, Spectradyne) was used for data analysis. Peak filter settings recommended by the manufacturer were used to differentiate signal from noise (signal/noise [S/N] > 10, diameter >130 nm, transit time <60 μs, peak symmetry index between 0.2 and 4.0, bin size of 10 nm). The particle size distribution and concentration were obtained from the provided analysis report.

Flow Cytometry (FCM). Fouling and stability testing were performed by measuring (1) the concentration of particles in a concentration of 95% plasma and (2) the fluorescence of fluorescently labeled protein solutions with a calibrated flow cytometer (A60-Micro, Apogee Flow Systems, Spain). Samples were measured for 120 s at a flow rate of 3.01 μL/min. The trigger was set at the side scattering detector using a threshold of 14 arbitrary units, corresponding to a side scattering cross section of 3 nm^2. Samples

https://doi.org/10.1021/acs.langmuir.5c03234
Langmuir 2025, 41, 33751−33760

Table 1. Size and Concentration of the Core of PS-NH_2 Colloidal Particles and Functionalized Colloidal Particles as Measured with Dynamic Light Scattering (DLS), Microfluidic Resistive Pulse Sensing (MRPS), and Cryogenic Electron Microscopy (Cryo-EM)[a]

	DLS		MRPS			cryo-EM
colloidal particle type	hydrodynamic diameter (nm)	polydispersity index	diameter (nm)	interquartile range (nm)	concentration (mL^{-1})	particle diameter (nm)
PS-NH_2	220 ± 2	0.01 ± 0.01	225	37	3.9×10^{12}	217 ± 8
PS-CPP	231 ± 3	0.02 ± 0.01	225	43	7.2×10^{11}	
PS-HPMA	260 ± 4	0.03 ± 0.01	225	32	1.1×10^{11}	221 ± 9
PS-MPC	250 ± 1	0.02 ± 0.02	235	33	1.1×10^{11}	224 ± 10
PS-CBMA	350 ± 5	0.2 ± 0.01	225	47	2.2×10^{10}	219 ± 11

[a]For DLS, the hydrodynamic diameter represents the median ± standard deviation of repetitive measurements. For MRPS, the numbers are based on the gated size distribution. For cryo-EM, the diameter represents the median ± standard deviation of the size distribution.

were diluted in DPBS to maintain a count rate below 10,000 counts per sec. The side scattering intensity was calibrated using Rosetta Calibration beads (Version 2.06, Exometry, The Netherlands). The obtained FCM data was analyzed using FlowJo software (Version 10.10.0). Details of the flow cytometry measurements can be found in the MIFlowCyt Supporting Information.

Cryogenic Electron Microscopy (Cryo-EM). Electron microscopy grids with holey carbon films (Quantifoil (Germany) 2/1, 300 mesh, copper) were glow-discharged in 0.2 mbar of air at 25 mA for 30 s (Pelco easiGlow (TED PELLA, USA)), after which 3 μL of sample was added to the grid. The sample was blotted away for 3 s using filter paper (Whatman no.1, Whatman, South Korea) at 95% humidity and room temperature, and the grid was subsequently plunged into liquid ethane/propane and kept at −196 °C (Leica EM GP (Leica, Germany)). Vitrified grids were clipped into autogrids and transferred to a Talos Arctica (ThermoFisher, USA) operated by EPU software (ThermoFisher, USA) in multigrid mode. From each sample, 200 movies were recorded by a K3 direct electron detector (Gatan Inc., USA) in counting mode and zero-loss-image (ZLP) imaging mode (20 eV) at a magnification of 15,000× (corresponding to a pixel size of 0.55 nm at specimen level), a defocus of −5 μm, and a total dose of 35 e/A^2. Movies were aligned using MotionCor2[31] and converted to tiff using EMAN2.[32]

Data was processed using the Fiji image processing package based on ImageJ2 (version 2.16.0). A rectangle measuring 500 pixels in width and 50 pixels in height was placed over each observed particle. The gray pixel profile of the selected rectangle was plotted. The change in gray value along the profile indicated a transition from background to particle. The start of the particle was identified by a sharp decrease in pixel intensity from the background level, and the end of the particle was marked by a return to background level intensity. The particle width in pixels was then processed by using the calibration value of 0.55 nm/pixel. This process was repeated for 5, 29, 30, and 33 particles for PS-NH_2, PS-HPMA, PS-MPC, and PS-CBMA, respectively.

Transmission Electron Microscopy (TEM). Prior to TEM imaging, samples were diluted 1000-fold in Milli-Q water and drop-cast (10 μL) onto copper grids, which were then air-dried for 2 h before measuring. TEM imaging was performed on a FEI Tecnai-12 120 kV (USA) transmission electron microscope equipped with a Lab6 filament, composite, and a Xarosa 5120 × 3840 pixel complementary metal oxide semiconductor bottom mount camera.

Protein Fouling and Stability. Plasma Labeling. To validate the antifouling capabilities of the functionalized colloidal particles, plasma proteins were labeled using AnaTag HiLyte Fluor 488 microscale protein labeling kit (AnaSpec). The manufacturer's instructions were followed using 100 μL of plasma per batch. The labeled protein sample was concentrated using 10 kDa centrifugal filter tubes (Millipore) at 4000 rpm for 30 min. The resulting concentrated protein sample was then diluted to a 10% solution using DPBS. The 10% solution resulted in a protein concentration of ∼ 5 mg/mL. Throughout this manuscript, the HiLyte Fluor 488 labeled plasma is named Plasma-HF488.

Protein Fouling. To study the protein fouling, solutions of 10% Plasma-HF488 (5 mg/mL) and 5 mg/mL of BSA-FITC were prepared. For each sample, 10 μL of the colloidal particles was added to 190 μL of protein solution, and the solutions were then incubated at 37 °C for 2 h. Colloidal particle solutions were vortexed, then dissolved 2000-fold and measured with a calibrated Apogee A60-micro FCM. Fluorescence intensity at 488 nm was analyzed using FlowJo.

Stability Measurements. The stability of the colloidal particles in protein solutions was measured using FCM. For each sample, 10 μL of the colloidal particles was added to 190 μL of plasma or DPBS. Samples were incubated at 37 °C for 0 to 5 h. Every hour, a sample was diluted 2000-fold and analyzed with a calibrated Apogee A60-Micro FCM. The flow cytometry data files were analyzed using FlowJo. The colloidal particles were gated by their measured side-scattering cross sections.

RESULTS & DISCUSSION

Functionalization and Characterization of the Colloidal Particles. *Size Determination.* To functionalize the colloidal particles with the RAFT agent (Scheme 1B), the prepared sulfo-NHS CPP was reacted with the amino groups present on the PS-NH_2 colloidal particles using standard NHS coupling chemistry at pH = 7.0. After RAFT-agent functionalization, the polymer brushes were grown from the colloidal particles using SI-PET-RAFT under irradiation with 410 nm light for 30, 15, and 5 min (HPMA, MPC, and CBMA, respectively).

Table 1 shows the diameters of the colloidal particles before and after brush formation, measured by DLS, MRPS, and cryo-EM. DLS obtained a diameter of 220 nm for the PS-NH_2 core, 231 nm for the RAFT-functionalized colloidal particles (PS-CPP), and 250 to 350 nm for the colloidal particles functionalized with polymer brushes. In contrast, MRPS and cryo-EM obtained diameters of 225 to 236 and 217 to 224 nm, respectively, for all colloidal particles, irrespective of their bareness or functionalization.

We attribute these differences in size to the nature of these measurement techniques. DLS obtained an increase in the diameter of colloidal particles with polymer brushes because DLS measures the hydrodynamic diameter, i.e., the effective diameter of perfect spheres that diffuse at the same rate as the measured particles in a fluid. The functionalization of the colloidal particles decreases their diffusion coefficient, resulting in an increase in the hydrodynamic diameter. In contrast, MRPS is based on the Coulter principle,[33] which estimates the diameter by measuring the electrical resistance of a particle passing through an aperture. As hydrated polymer brushes in a conductive aqueous environment probably offer negligible

https://doi.org/10.1021/acs.langmuir.5c03234
Langmuir 2025, 41, 33751−33760

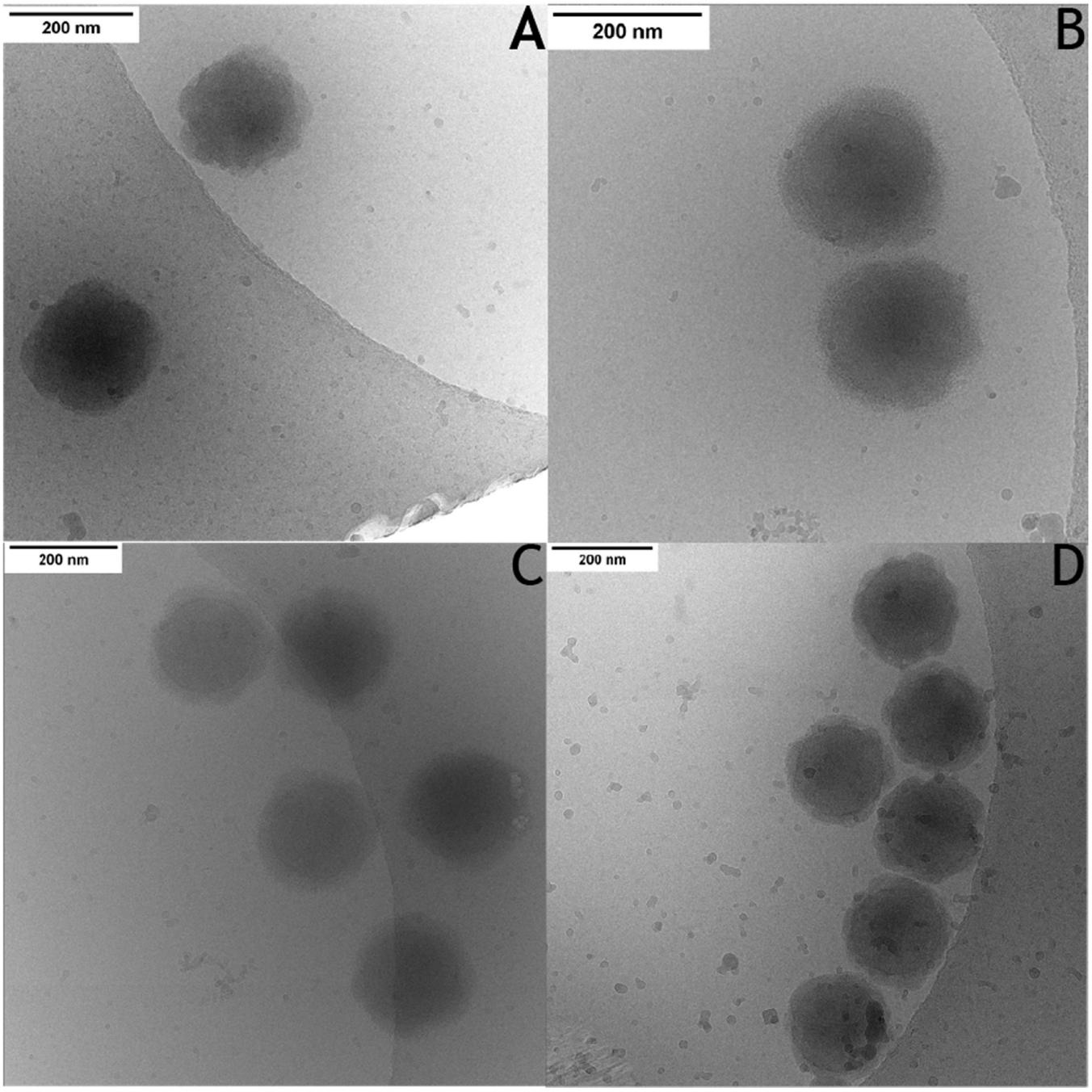

Figure 1. Cryo-electron microscopy images of functionalized colloidal particles. (A) PS-NH_2. (B) PS-HPMA. (C) PS-MPC. (D) PS-CBMA. The electron dense core is surrounded by a less dense shell-system, resulting in an apparent core−shell structure.

electrical resistance, MRPS will likely primarily sense the core of the colloidal particles, which is in line with our observations. Cryo-EM also measured particle sizes smaller than those of DLS. Figure 1 shows cryo-EM images of the PS-NH_2 core (Figure 1A) and functionalized colloidal particles (Figure 1B-D). For the functionalized colloidal particles, a core−shell-like structure is visible, whereas the shell is absent for the PS-NH_2 colloidal particles. The small increase in diameter of the functionalized colloidal particles compared to the PS-NH_2 colloidal particles might be due to insufficient imaging contrast between the vitrified water and the hydrated polymer brushes, which have similar electron density. The lack of imaging contrast results in only the core of the particle being measured, and this is reported in Table 1.

As a measure of dispersion, Table 1 also shows the polydispersity index obtained by DLS, the interquartile range obtained by MRPS, and the standard deviation for cryo-EM. The results show that colloidal particles with HPMA and MPC brushes were monodisperse, whereas colloidal particles with CBMA brushes were polydisperse. Owing to their high reaction rate,[34] CBMA particles develop longer polymer brushes, thereby increasing the contrast between the hydrodynamic diameter measured with DLS and the core diameter measured with MRPS and cryo-EM relative to the other particles.

https://doi.org/10.1021/acs.langmuir.5c03234
Langmuir 2025, 41, 33751−33760

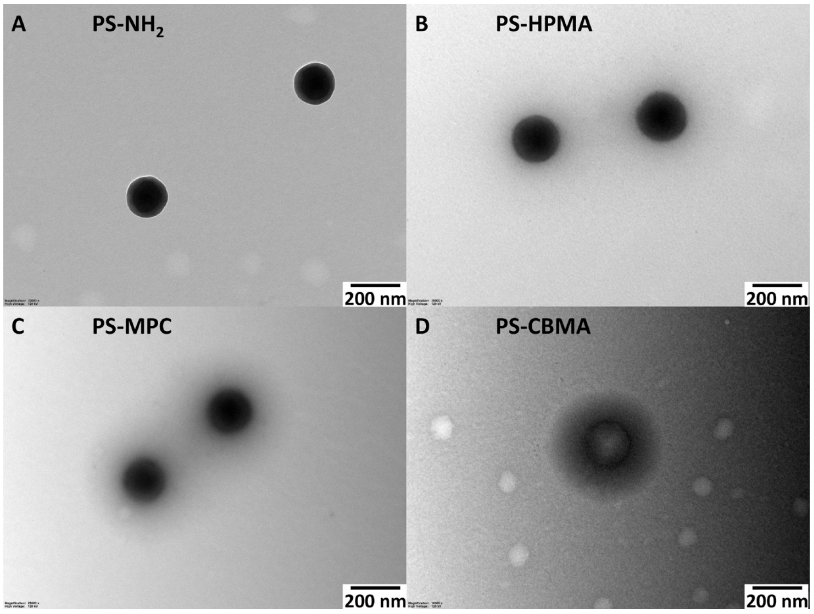

Figure 2. Transmission electron microscopy images were obtained of the functionalized colloidal particles. (A) PS-NH_2. (B) PS-HPMA. (C) PS-MPC. (D) PS-CBMA. The brushes are surrounding the core in a gradient of electron density, revealing a core−shell structure.

Concentration Determination. Table 1 also shows that the concentration of PS-NH_2 colloidal particles is 3.9×10^{12} mL^{-1}, which is similar to the concentration of $4-5 \times 10^{12}$ mL^{-1} mentioned by the manufacturer. A concentration of $\sim 10^{12}$ particles for PS-CPP is expected, considering the 10-fold dilution used for the functionalization. MRPS obtained a concentration of $2 \times 10^{10} - 1 \times 10^{11}$ mL^{-1} for the functionalized colloidal particles.

Morphology. To investigate the shell of the functionalized colloidal particles in more detail, conventional TEM imaging at room temperature was used. Figure 2 shows TEM images of the PS-NH_2 core and functionalized colloidal particles. Figure 2A shows that the PS-NH_2 colloidal particles have a clear round structure, i.e., without brushes. In Figure 2B−D, the core is surrounded by a halo. As polymer brushes collapse during dehydration and fixation, they form dense, compact layers around the beads. Compared to cryo-EM, this collapsed structure has a higher electron density and better contrast against the vacuum background and, hence, becomes visible as a gradient. For the zwitterionic PS-MPC and PS-CBMA colloidal particles (Figure 2C,D), the brushes are better visible than for the nonzwitterionic PS-HPMA colloidal particles (Figure 2B).

Chemical Characterization. To determine the chemical composition of the colloidal particles, Figure 3 shows an XPS wide scan analysis. Compared with the PS-NH_2 colloidal particles, which form the core for all other colloidal particles, PS-CPP colloidal particles show an increase in sulfur contents as expected for RAFT-agent functionalization. Subsequent functionalization of the PS-CPP colloidal particles with the polymer brushes shows the expected decrease in sulfur (none of the three monomers contains sulfur), and an increase in carbon, nitrogen, and oxygen, as would be expected based on the atomic composition of the monomers. Based on the DLS data, the wet brush thickness for PS-HPMA and PS-MPC is about 12−15 nm, corresponding to a dry thickness (as effective in XPS) of about 5 nm. This not only yields the unattenuated transmission of the PS core, with a concomitantly large %C,

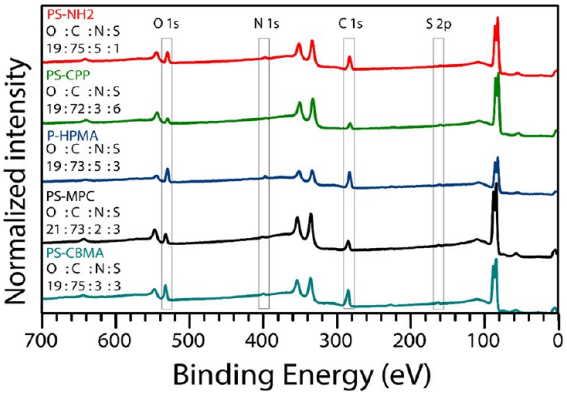

Figure 3. Wide-scan X-ray photoelectron spectroscopy data for all colloidal particle types. From top to bottom: PS-NH_2 core colloidal particle (red), PS-CPP RAFT functionalized colloidal particles (green), PS-HPMA functionalized colloidal particles (blue), PS-MPC functionalized colloidal particles (black), and PS-CBMA functionalized colloidal particles (cyan). The phosphorus signal of MPC is undetectable because its weak intensity is masked by the dominant carbon background.

here, 72−75% in all cases, but also implies that the weak signal, like the phosphorus peak in PS-MPC, is not observed.

Figure 4 shows the C 1s XPS narrow-scan of the PS-NH_2 core (Figure 4A) and the functionalized colloidal particles (Figure 4B−D), revealing distinguishable peaks corresponding to C═O of the carbonyl at 288.6 eV, heteroatoms C−O/C−N carbon atoms at 286.3 eV, and C−C carbon atoms at 385.0 eV. All of these bonds are expected for the produced colloidal particles. The most notable difference between the core structure and the functionalized colloidal particles is the increase in C═O presence, which is attributed to the growth of polymer brushes containing methacrylate and methacrylamide. In addition, a decrease in the heteroatom to carbon ratio is observed, which is expected for growing polymer brushes due to the increase in carbon content during the growth of the polymer brushes.

https://doi.org/10.1021/acs.langmuir.5c03234
Langmuir 2025, 41, 33751−33760

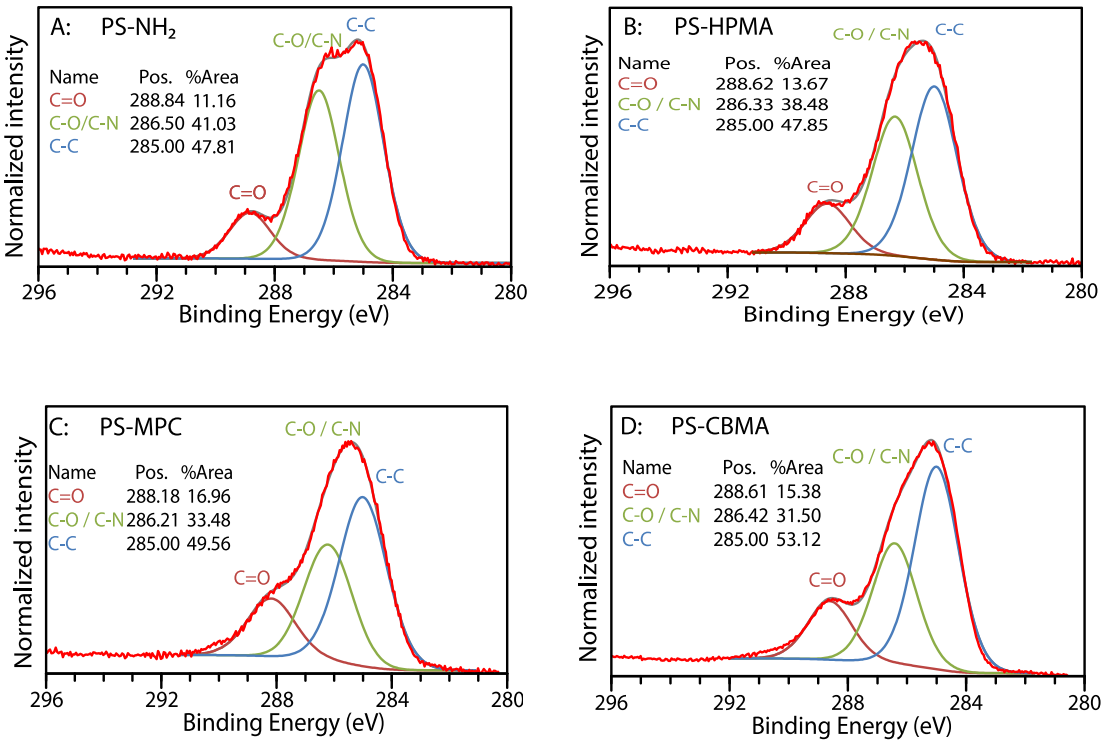

Figure 4. XPS C 1s narrow scan of the PS-NH_2 core and functionalized colloidal particles. (A) PS-NH_2, (B) PS-HPMA, (C) PS-MPC, and (D) PS-CBMA. The fits distinguish three peaks corresponding to C═O (red), C−O/C−N (heteroatom; green), and C−C (blue).

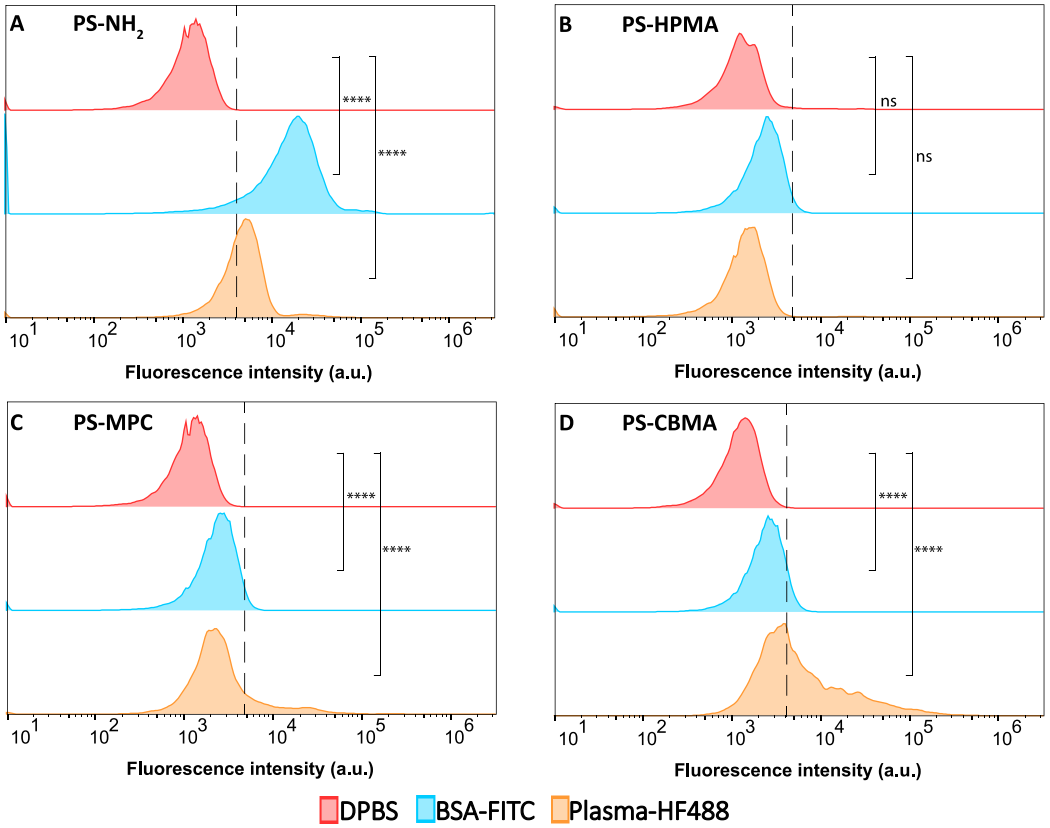

Figure 5. Fluorescence positivity as a measure of biofouling. (A) PS-NH_2, (B) PS-HPMA, (C) PS-MPC, and (D) PS-CBMA. From top to bottom: incubation in Dulbecco's phosphate-buffered saline (DPBS; red), BSA-FITC (5 mg/mL; blue), or 10% plasma-HF488 (5 mg/mL; orange). The threshold for fluorescence positivity (dotted line) was defined as the median plus 4 times the standard deviation of the fluorescence intensity histogram of the DPBS control measurement. Amplitude of the histograms was normalized to their modes.

https://doi.org/10.1021/acs.langmuir.5c03234
Langmuir 2025, 41, 33751−33760

Antifouling Properties and Stability of the Functionalized Colloidal Particles. *Antifouling Properties.* To evaluate the antifouling properties of the functionalized colloidal particles, two different protein solutions were selected: a single-protein solution consisting of 5 mg/mL bovine serum albumin fluorescein isothiocyanate (BSA-FITC), and a complex protein solution in the form of a 10% plasma solution (plasma-HF488). All three functionalized colloidal particles, as well as the PS-NH_2 core, were exposed to BSA-FITC, plasma-HF488, and DPBS for 2 h. Figure 5A–D shows the relative fluorescence intensities of PS-NH_2, PS-HPMA, PS-MPC, and PS-CBMA, respectively, measured with FCM.

Samples with the PS-NH_2 core showed increased fluorescence for both the BSA-FITC solution and the plasma-HF488 solution compared to DPBS (Figure 5A), indicating that proteins have adsorbed onto the surface of the colloidal particle. In contrast, the three functionalized colloidal particles showed no or negligible fluorescence positivity in the BSA-FITC solution (Figure 5B–D), demonstrating effective antifouling properties. However, the main aim is to achieve stability in 10% plasma. In the plasma-HF488 solution, PS-HPMA showed no increase in fluorescence intensity (Figure 5B), PS-MPC showed a slight increase (Figure 5C), and PS-CBMA showed a relatively high increase compared to that of DPBS (Figure 5D). This finding indicates that the antifouling effectiveness followed the order of PS-HPMA > PS-MPC > PS-CBMA. The relatively poor antifouling properties of the PS-CBMA colloidal particles can be explained by their polydispersity, which suggests the presence of under-modified colloidal particles, which are expected to adsorb proteins.

Stability. To investigate the stability of the colloidal particles, the concentrations of colloidal particles were measured in DPBS. In addition, the PS-NH_2 cores were also measured in 10% plasma, while the functionalized colloidal particles, which were expected to be able to withstand some harsher fouling conditions, were measured in 95% plasma. The colloidal particles were analyzed hourly by FCM for a period of 5 h.

Figure 6A shows the concentration of the PS-NH_2 core colloidal particles in DPBS versus time, revealing a 10% loss in concentration. However, in 10% plasma, the concentration of the PS-NH_2 core decreases over time, as shown in Figure 6B, revealing a 70% decrease in concentration. We attribute the decrease in plasma to protein fouling, which causes rapid aggregation of the colloidal particles. Figure 6C shows the stability of HPMA-, MPC-, and CBMA-functionalized colloidal particles in DPBS. Both zwitterionic monomers show a stable trend, whereas the PS-HPMA colloidal particles decrease in concentration over time. The stable trend of the zwitterionic functionalized colloidal particles is attributed to a more stable stern-layer compared to the nonzwitterionic PS-HPMA.

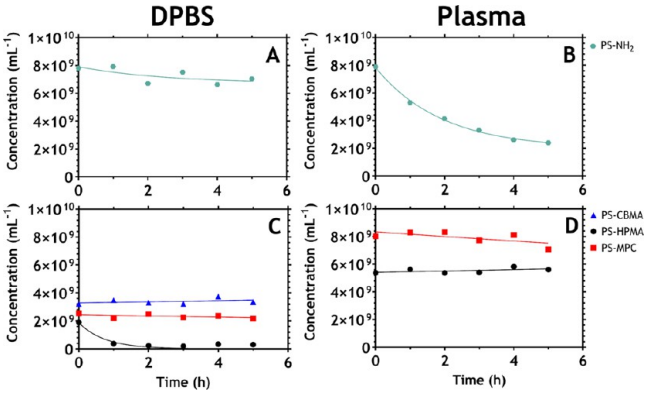

Figure 6. Stability of colloidal particles in plasma and Dulbecco's phosphate-buffered saline (DPBS). (A) PS-NH_2 core in DPBS, (B) PS-NH_2 core in 10% plasma, (C) functionalized colloidal particles in DPBS, and (D) functionalized colloidal particles in 95% plasma. Panel (B) lacks PS-CBMA because no particles exceeded the noise-threshold.

Figure 6D shows the stability of PS-MPC and PS-HPMA in 95% plasma. Both these functionalized colloidal particles show a stable trend over time. The PS-CBMA colloidal particles are missing because they did not exceed the noise threshold after time point 0 h, indicating that PS-CBMA colloidal particles are unstable in 95% plasma. This result was expected because the PS-CBMA colloidal particles showed fouling during the fouling experiment (Figure 5D). This means that proteins will adsorb onto the surface of the PS-CBMA colloidal particles. This leads to decreased stability caused by rapid aggregation.

CONCLUSIONS

Polystyrene colloidal particles can be effectively functionalized with both nonzwitterionic and zwitterionic polymer brushes using SI-PET-RAFT under aqueous, oxygen-tolerant conditions. The colloidal particle size growth was verified using DLS, functionalization was confirmed through XPS, and brushes were visualized using TEM. Antifouling properties of the colloidal particles were validated in both BSA single-protein solution and plasma, with stability when spiked into pure plasma. PS-HPMA performed best with regard to antifouling properties and time stability in plasma, followed by PS-MPC, and then PS-CBMA. PS-CBMA showed no stability in a concentration of 95% plasma but performed similarly in bovine serum albumin solution to the other monomers. The performance of PS-HPMA and PS-MPC is consistent with previously reported data by Van Andel et al.,[26] whereas PS-CBMA performed less well than previously described.

The development of mass-production-compatible colloidal particles that are stable in high-concentration plasma shows promise for further research in biomedical fields. Particularly, instruments for the detection of nanoparticle concentrations, such as flow cytometers to study EVs, and also single-particle inductively coupled plasma mass spectrometry, nanoparticle tracking analysis, and microfluidic resistive pulse sensing might benefit from colloidal particles as internal calibrants or quality controls.

Future use of these colloidal particles should include a metrologically traceable procedure to assign a concentration with uncertainty to the produced colloidal particles. This can then, in turn, improve measurements of nanoparticle concentrations.

ASSOCIATED CONTENT

Supporting Information

The Supporting Information is available free of charge at https://pubs.acs.org/doi/10.1021/acs.langmuir.5c03234.

Minimum information required to reproduce the flow cytometry experiments on colloidal particles performed in this study (PDF)

https://doi.org/10.1021/acs.langmuir.5c03234
Langmuir 2025, 41, 33751−33760

AUTHOR INFORMATION

Corresponding Authors

Jelle B.J. van den Beukel − *Biomedical Engineering & Physics, Amsterdam UMC, University of Amsterdam, Amsterdam 1105 AZ, The Netherlands; Laboratory of Experimental Clinical Chemistry, Laboratory Specialized Diagnostics & Research, Department of Laboratory Medicine, Amsterdam 1105 AZ, The Netherlands; Cancer Center Amsterdam, Imaging and Biomarkers, Amsterdam 1105 AZ, The Netherlands; Amsterdam Cardiovascular Sciences, Amsterdam 1105 AZ, The Netherlands; Laboratory of Organic Chemistry, Wageningen University and Research, Wageningen 6708WE, The Netherlands;* orcid.org/0000-0002-9844-2426; Email: j.b.j.vandenbeukel@amsterdamumc.nl

Han Zuilhof − *Laboratory of Organic Chemistry, Wageningen University and Research, Wageningen 6708WE, The Netherlands; School of Pharmaceutical Science and Technology, Tianjin University, Tianjin 300072, China; College of Biological and Chemical Sciences, Jiaxing University, Jiaxing 314001, China;* orcid.org/0000-0001-5773-8506; Email: han.zuilhof@wur.nl

Authors

Barend van Lagen − *Laboratory of Organic Chemistry, Wageningen University and Research, Wageningen 6708WE, The Netherlands;* orcid.org/0000-0003-1201-8569

Edwin van der Pol − *Biomedical Engineering & Physics, Amsterdam UMC, University of Amsterdam, Amsterdam 1105 AZ, The Netherlands; Laboratory Specialized Diagnostics & Research, Department of Laboratory Medicine, Laboratory of Experimental Clinical Chemistry, Amsterdam 1105 AZ, The Netherlands; Imaging and Biomarkers, Cancer Center Amsterdam, Amsterdam 1105 AZ, The Netherlands; Amsterdam Cardiovascular Sciences, Amsterdam 1105 AZ, The Netherlands;* orcid.org/0000-0002-9497-8426

Complete contact information is available at: https://pubs.acs.org/10.1021/acs.langmuir.5c03234

Funding

J.B.J.v.d.B and E.v.d.P. acknowledge funding from the Dutch Research Council (NWO), VIDI 19724, and H.Z. from a Top-level Talent Project of Zhejiang Province (Jiaxing University).

Notes

The authors declare the following competing financial interest(s): Edwin van der Pol is a co-founder and shareholder of Exometry B.V., Amsterdam, The Netherlands.

[†]Co-author B.v.L. has sadly passed away during the writing process.

ACKNOWLEDGMENTS

The authors thank Chi Hau, Mandy Los, Remko Fokkink, and Sidharam Pujari for insightful discussions and technical assistance. Dr Roman Koning of the electron microscopy facility from Leiden University Medical Center is thanked for his Cryo-EM support. Anita Grootemaat and Irene Schimmel from Amsterdam Medical Center's Cellular Imaging department are thanked for their TEM support. Paul Bloemen is thanked for his assistance in the making of the LED setup. Mona Shahsavari is thanked for her assistance with MRPS data. Dr. Britta Bettin is thanked for her assistance with MyFloCyte.

REFERENCES

(1) Barile, L.; Vassalli, G. Exosomes: Therapy Delivery Tools and Biomarkers of Diseases. *Pharmacol. Ther.* **2017**, *174*, 63−78.

(2) Bernardi, S.; Balbi, C. Extracellular Vesicles: From Biomarkers to Therapeutic Tools. *Biology* **2020**, *9* (9), 258.

(3) Welsh, J. A.; Arkesteijn, G. J. A.; Bremer, M.; Cimorelli, M.; Dignat-George, F.; Giebel, B.; Görgens, A.; Hendrix, A.; Kuiper, M.; Lacroix, R.; Lannigan, J.; van Leeuwen, T. G.; Lozano-Andrés, E.; Rao, S.; Robert, S.; de Rond, L.; Tang, V. A.; Tertel, T.; Yan, X.; Wauben, M. H. M.; Nolan, J. P.; Jones, J. C.; Nieuwland, R.; van der Pol, E. A Compendium of Single Extracellular Vesicle Flow Cytometry. *J. Extracell. Vesicles* **2023**, *12* (2), No. e12299.

(4) Welsh, J. A.; Goberdhan, D. C. I.; O'Driscoll, L.; Buzas, E. I.; Blenkiron, C.; Bussolati, B.; Cai, H.; Di Vizio, D.; Driedonks, T. A. P.; Erdbrügger, U.; Falcon-Perez, J. M.; Fu, Q.; Hill, A. F.; Lenassi, M.; Lim, S. K.; Mahoney, M. G.; Mohanty, S.; Möller, A.; Nieuwland, R.; Ochiya, T.; Sahoo, S.; Torrecilhas, A. C.; Zheng, L.; Zijlstra, A.; Abuelreich, S.; Bagabas, R.; Bergese, P.; Bridges, E. M.; Brucale, M.; Burger, D.; Carney, R. P.; Cocucci, E.; Crescitelli, R.; Hanser, E.; Harris, A. L.; Haughey, N. J.; Hendrix, A.; Ivanov, A. R.; Jovanovic-Talisman, T.; Kruh-Garcia, N. A.; Ku'ulei-Lyn Faustino, V.; Kyburz, D.; Lässer, C.; Lennon, K. M.; Lötvall, J.; Maddox, A. L.; Martens-Uzunova, E. S.; Mizenko, R. R.; Newman, L. A.; Ridolfi, A.; Rohde, E.; Rojalin, T.; Rowland, A.; Saftics, A.; Sandau, U. S.; Saugstad, J. A.; Shekari, F.; Swift, S.; Ter-Ovanesyan, D.; Tosar, J. P.; Useckaite, Z.; Valle, F.; Varga, Z.; Van Der Pol, E.; Van Herwijnen, M. J. C.; Wauben, M. H. M.; Wehman, A. M.; Williams, S.; Zendrini, A.; Zimmerman, A. J.; MISEV Consortium; Théry, C.; Witwer, K. W. Minimal Information for Studies of Extracellular Vesicles (MISEV2023): From Basic to Advanced Approaches. *J. Extracell. Vesicles* **2024**, *13* (2), No. e12404.

(5) Van Der Pol, E.; Coumans, F. A. W.; Grootemaat, A. E.; Gardiner, C.; Sargent, I. L.; Harrison, P.; Sturk, A.; Van Leeuwen, T. G.; Nieuwland, R. Particle Size Distribution of Exosomes and Microvesicles Determined by Transmission Electron Microscopy, Flow Cytometry, Nanoparticle Tracking Analysis, and Resistive Pulse Sensing. *J. Thromb. Haemost.* **2014**, *12* (7), 1182−1192.

(6) Nieuwland, R.; Siljander, P. R. A Beginner's Guide to Study Extracellular Vesicles in Human Blood Plasma and Serum. *J. Extracell. Vesicles* **2024**, *13* (1), No. e12400.

(7) Yuana, Y.; Böing, A. N.; Grootemaat, A. E.; Van Der Pol, E.; Hau, C. M.; Cizmar, P.; Buhr, E.; Sturk, A.; Nieuwland, R. Handling and Storage of Human Body Fluids for Analysis of Extracellular Vesicles. *J. Extracell. Vesicles* **2015**, *4* (1), No. 29260.

(8) EV-TRACK Consortium; Van Deun, J.; Mestdagh, P.; Agostinis, P.; Akay, Ö.; Anand, S.; Anckaert, J.; Martinez, Z. A.; Baetens, T.; Beghein, E.; Bertier, L.; Berx, G.; Boere, J.; Boukouris, S.; Bremer, M.; Buschmann, D.; Byrd, J. B.; Casert, C.; Cheng, L.; Cmoch, A.; Daveloose, D.; De Smedt, E.; Demirsoy, S.; Depoorter, V.; Dhondt, B.; Driedonks, T. A. P.; Dudek, A.; Elsharawy, A.; Floris, I.; Foers, A. D.; Gärtner, K.; Garg, A. D.; Geeurickx, E.; Gettemans, J.; Ghazavi, F.; Giebel, B.; Kormelink, T. G.; Hancock, G.; Helsmoortel, H.; Hill, A. F.; Hyenne, V.; Kalra, H.; Kim, D.; Kowal, J.; Kraemer, S.; Leidinger, P.; Leonelli, C.; Liang, Y.; Lippens, L.; Liu, S.; Lo Cicero, A.; Martin, S.; Mathivanan, S.; Mathiyalagan, P.; Matusek, T.; Milani, G.; Monguió-Tortajada, M.; Mus, L. M.; Muth, D. C.; Németh, A.; Nolte-'t Hoen, E. N. M.; O'Driscoll, L.; Palmulli, R.; Pfaffl, M. W.; Primdal-Bengtson, B.; Romano, E.; Rousseau, Q.; Sahoo, S.; Sampaio, N.; Samuel, M.; Scicluna, B.; Soen, B.; Steels, A.; Swinnen, J. V.; Takatalo, M.; Thaminy, S.; Théry, C.; Tulkens, J.; Van Audenhove, I.; Van Der Grein, S.; Van Goethem, A.; Van Herwijnen, M. J.; Van Niel, G.; Van Roy, N.; Van Vliet, A. R.; Vandamme, N.; Vanhauwaert, S.; Vergauwen, G.; Verweij, F.; Wallaert, A.; Wauben, M.; Witwer, K. W.; Zonneveld, M. I.; De Wever, O.; Vandesompele, J.; Hendrix, A. EV-TRACK: Transparent Reporting and Centralizing Knowledge in Extracellular Vesicle Research. *Nat. Methods* **2017**, *14* (3), 228−232.

(9) Vogel, R.; Savage, J.; Muzard, J.; Della Camera, G.; Vella, G.; Law, A.; Marchioni, M.; Mehn, D.; Geiss, O.; Peacock, B.; Aubert, D.; Calzolai, L.; Caputo, F.; Prina-Mello, A. Measuring Particle

Concentration of Multimodal Synthetic Reference Materials and Extracellular Vesicles with Orthogonal Techniques: Who Is up to the Challenge? *J. Extracell. Vesicles* **2021**, *10* (3), No. e12052.
(10) García-Álvarez, R.; Vallet-Regí, M. Hard and Soft Protein Corona of Nanomaterials: Analysis and Relevance. *Nanomaterials* **2021**, *11* (4), 888.
(11) Wheeler, K. E.; Chetwynd, A. J.; Fahy, K. M.; Hong, B. S.; Tochihuitl, J. A.; Foster, L. A.; Lynch, I. Environmental Dimensions of the Protein Corona. *Nat. Nanotechnol.* **2021**, *16* (6), 617−629.
(12) Shemetov, A. A.; Nabiev, I.; Sukhanova, A. Molecular Interaction of Proteins and Peptides with Nanoparticles. *ACS Nano* **2012**, *6* (6), 4585−4602.
(13) Hajipour, M. J.; Safavi-Sohi, R.; Sharifi, S.; Mahmoud, N.; Ashkarran, A. A.; Voke, E.; Serpooshan, V.; Ramezankhani, M.; Milani, A. S.; Landry, M. P.; Mahmoudi, M. An Overview of Nanoparticle Protein Corona Literature. *Small* **2023**, *19* (36), No. 2301838.
(14) Ge, C.; Tian, J.; Zhao, Y.; Chen, C.; Zhou, R.; Chai, Z. Towards Understanding of Nanoparticle-Protein Corona. *Arch. Toxicol.* **2015**, *89* (4), 519−539.
(15) Oberländer, J.; Champanhac, C.; Da Costa Marques, R.; Landfester, K.; Mailänder, V. Temperature, Concentration, and Surface Modification Influence the Cellular Uptake and the Protein Corona of Polystyrene Nanoparticles. *Acta Biomater.* **2022**, *148*, 271−278.
(16) Lundqvist, M.; Stigler, J.; Elia, G.; Lynch, I.; Cedervall, T.; Dawson, K. A. Nanoparticle Size and Surface Properties Determine the Protein Corona with Possible Implications for Biological Impacts. *Proc. Natl. Acad. Sci. U. S. A.* **2008**, *105* (38), 14265−14270.
(17) Gessner, A.; Lieske, A.; Paulke, B.; Müller, R. H. Functional Groups on Polystyrene Model Nanoparticles: Influence on Protein Adsorption. *J. Biomed. Mater. Res., Part A* **2003**, *65A* (3), 319−326.
(18) Li, Q.; Wen, C.; Yang, J.; Zhou, X.; Zhu, Y.; Zheng, J.; Cheng, G.; Bai, J.; Xu, T.; Ji, J.; Jiang, S.; Zhang, L.; Zhang, P. Zwitterionic Biomaterials. *Chem. Rev.* **2022**, *122* (23), 17073−17154.
(19) Teunissen, L. W.; Van Den Beukel, J.; Smulders, M. M. J.; Zuilhof, H. Thermoresponsive Polymer Brushes for Switchable Protein Adsorption via Dopamine-Assisted Grafting-To Strategy. *Adv. Mater. Interfaces* **2022**, *9* (33), No. 2201198.
(20) Ionov, L.; Zdyrko, B.; Sidorenko, A.; Minko, S.; Klep, V.; Luzinov, I.; Stamm, M. Gradient Polymer Layers by "Grafting To" Approach. *Macromol. Rapid Commun.* **2004**, *25* (1), 360−365.
(21) Kuzmyn, A. R.; Nguyen, A. T.; Teunissen, L. W.; Zuilhof, H.; Baggerman, J. Antifouling Polymer Brushes via Oxygen-Tolerant Surface-Initiated PET-RAFT. *Langmuir* **2020**, *36* (16), 4439−4446.
(22) Kuzmyn, A. R.; De Los Santos Pereira, A.; Pop-Georgievski, O.; Bruns, M.; Brynda, E.; Rodriguez-Emmenegger, C. Exploiting End Group Functionalization for the Design of Antifouling Bioactive Brushes. *Polym. Chem.* **2014**, *5* (13), 4124−4131.
(23) Baggerman, J.; Smulders, M. M. J.; Zuilhof, H. Romantic Surfaces: A Systematic Overview of Stable, Biospecific, and Antifouling Zwitterionic Surfaces. *Langmuir* **2019**, *35* (5), 1072−1084.
(24) Rungta, A.; Natarajan, B.; Neely, T.; Dukes, D.; Schadler, L. S.; Benicewicz, B. C. Grafting Bimodal Polymer Brushes on Nanoparticles Using Controlled Radical Polymerization. *Macromolecules* **2012**, *45* (23), 9303−9311.
(25) Van Andel, E.; De Bus, I.; Tijhaar, E. J.; Smulders, M. M. J.; Savelkoul, H. F. J.; Zuilhof, H. Highly Specific Binding on Antifouling Zwitterionic Polymer-Coated Microbeads as Measured by Flow Cytometry. *ACS Appl. Mater. Interfaces* **2017**, *9* (44), 38211−38221.
(26) Van Andel, E.; Lange, S. C.; Pujari, S. P.; Tijhaar, E. J.; Smulders, M. M. J.; Savelkoul, H. F. J.; Zuilhof, H. Systematic Comparison of Zwitterionic and Non-Zwitterionic Antifouling Polymer Brushes on a Bead-Based Platform. *Langmuir* **2019**, *35* (5), 1181−1191.
(27) Fors, B. P.; Hawker, C. J. Control of a Living Radical Polymerization of Methacrylates by Light. *Angew. Chem., Int. Ed.* **2012**, *51* (35), 8850−8853.
(28) Kuzmyn, A. R.; Van Galen, M.; Van Lagen, B.; Zuilhof, H. SI-PET-RAFT in Flow: Improved Control over Polymer Brush Growth. *Polym. Chem.* **2023**, *14* (29), 3357−3363.
(29) Chen, H.; Zhao, C.; Zhang, M.; Chen, Q.; Ma, J.; Zheng, J. Molecular Understanding and Structural-Based Design of Polyacrylamides and Polyacrylates as Antifouling Materials. *Langmuir* **2016**, *32* (14), 3315−3330.
(30) Fairley, N.; Fernandez, V.; Richard-Plouet, M.; Guillot-Deudon, C.; Walton, J.; Smith, E.; Flahaut, D.; Greiner, M.; Biesinger, M.; Tougaard, S.; Morgan, D.; Baltrusaitis, J. Systematic and Collaborative Approach to Problem Solving Using X-Ray Photoelectron Spectroscopy. *Appl. Surf. Sci. Adv.* **2021**, *5*, No. 100112.
(31) Zheng, S. Q.; Palovcak, E.; Armache, J.-P.; Verba, K. A.; Cheng, Y.; Agard, D. A. MotionCor2: Anisotropic Correction of Beam-Induced Motion for Improved Cryo-Electron Microscopy. *Nat. Methods* **2017**, *14* (4), 331−332.
(32) Tang, G.; Peng, L.; Baldwin, P. R.; Mann, D. S.; Jiang, W.; Rees, I.; Ludtke, S. J. EMAN2: An Extensible Image Processing Suite for Electron Microscopy. *J. Struct. Biol.* **2007**, *157* (1), 38−46.
(33) Fraikin, J.-L.; Teesalu, T.; McKenney, C. M.; Ruoslahti, E.; Cleland, A. N. A High-Throughput Label-Free Nanoparticle Analyser. *Nat. Nanotechnol.* **2011**, *6* (5), 308−313.
(34) Kuzmyn, A. R.; Teunissen, L. W.; Fritz, P.; van Lagen, B.; Smulders, M. M. J.; Zuilhof, H. Diblock and Random Antifouling Bioactive Polymer Brushes on Gold Surfaces by Visible-Light-Induced Polymerization (SI-PET-RAFT) in Water. *Adv. Mater. Interfaces* **2022**, *9* (3), 1−12.

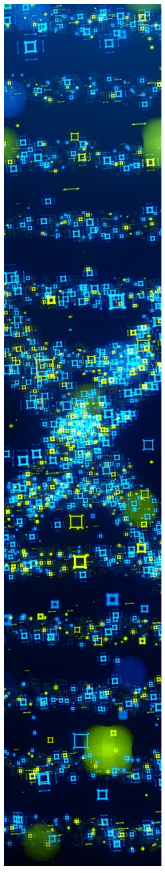

https://doi.org/10.1021/acs.langmuir.5c03234
Langmuir 2025, 41, 33751−33760